Effect of Crystallization Kinetics on the Properties of Spray Dried Microparticles

Alberto Baldelli[1], *Rory M. Power*[2,3], *Rachael E. H. Miles*[2], *Jonathan P. Reid*[2], *Reinhard Vehring*[1]

Department of Mechanical Engineering
4-9 Mechanical Engineering Building
University of Alberta
Edmonton, AB, T6G 2G8, Canada

Keywords: Particle engineering, Drug delivery, Particle formation, Crystallization process, Structured microparticles, Sodium nitrate

[1] Corresponding author: Department of Mechanical Engineering, University of Alberta, Edmonton, AB T6G 2G8, Canada.

[2] School of Chemistry, University of Bristol, Bristol, BS8 1TS, U.K.

[3] Now at:Max Planck Institute of Molecular Cell Biology and Genetics, Dresden, 01307, Germany.

Abstract

A droplet chain technique was used to study the influence of the crystallization process on the morphology of spray dried microparticles. A piezoceramic dispenser produced a chain of monodisperse solution droplets with an initial diameter in the range of 60 to 80 µm. Aqueous solutions of sodium nitrate were prepared in concentrations ranging from 5 mg/ml to $5 \cdot 10^{-5}$ mg/ml. The solution droplets were injected into a laminar flow with gas temperatures varying from 25 to 150 °C, affecting the droplet temperature and the evaporation rate, accordingly. Dried particles with diameters between 0.3 and 18 µm were collected. The properties of the collected microparticles were studied and correlated with a particle formation model which predicted the onset of saturation and crystallization. The model accounted for the dependence of the diffusion coefficient of sodium nitrate in water on droplet viscosity. The viscosity trend for sodium nitrate solutions was determined by studying the relaxation time observed during coalescence of two aqueous sodium nitrate droplets levitated in optical tweezers. The combination of theoretical derivations and experimental results showed that longer time available for crystallization correlates with larger crystal size and higher degrees of crystallinity in the final microparticles.

INTRODUCTION

Respiratory drug delivery allows solid microparticles, in the range of 0.1 to 5 µm, to be deposited in the patients' lungs (Garcia et al. 2012; Wachtel 2016). The advantages of delivering drugs via inhalation are multiple: high concentration of the drugs delivered to the disease site, minimal risks of side effects, rapid clinical response, low drug loss during the delivery compared to other techniques, and non-invasive treatment (Courrier et al. 2002). Despite the strong interest in respiratory drug delivery, an understanding of the impacts of the properties of microparticles on delivery efficiency and efficacy is not well defined (Labiris and Dolovich 2003). An example of important properties of microparticles is the diameter. The smaller the particles are, the deeper they can reach; the effect can change according to the type of microparticles involved (Everard et al. 1992). Other properties can be considered relevant; morphology and crystallinity are main factors in the efficiency of the drug delivery (Beck-Broichsitter et al. 2012; Park et al. 2013; Zhu et al. 2014). It has been shown that particles with high roughness reduce cohesion forces and, therefore, improve powder dispersibility (Hoe et al. 2014). Drugs can exist in different solid phases: amorphous, crystalline, or a mixture of them. Each phase can present different properties fundamental for pharmaceutical studies; the relationship between the properties and the solid

phase can vary accordingly to which chemical compound the microparticles are made of (Byrn et al. 1994; Sou et al. 2013). For example, it has been found that crystalline proteins remain more stable during the delivery compared to amorphous proteins (Elkordy et al. 2004). In addition, crystalline drugs are more commonly used due to their thermodynamic stability. On the other hand, amorphous spray-dried drugs may have a smaller and more homogenous particle size and a higher respirable fraction than mechanically micronized particles (Steckel et al. 2003). The dependence of the performance of pulmonary drugs on their solid phase highlights the need to understand particle formation and crystallization process. The main goal of particle engineering is to understand particle formation process in order to control the properties of the produced microparticles (Ticehurst and Marziano 2015). The particle formation process is the transition between solution droplets to dried particles (Vicente et al. 2013). During this process, one of two development options is encountered: the solvent and solute remain homogenously mixed or they separate creating core-shell or solid particles (Baldelli et al. 2015). If the chosen solute can crystallize, the particle formation process may also involve two sub-processes related to crystallization, i.e. crystal nucleation and crystal growth. (Ye et al. 2015).

Studies on particle formation focus mainly on the first part of the process that can be modeled as evaporation of a solution droplet (Boraey and Vehring 2014; Bück et al. 2015; Gradon and Sosnowski 2014). The solvent evaporation phase plays an important role in the particle formation process (Paudel et al. 2013). However, few experimental methods are currently available for the study and the evaluation of the particle formation process, and specifically, of the crystallization process of a solution droplet. The main three methods use: droplets suspended on a thin filament (Al Zaitone and Tropea 2011; Duprat et al. 2013; Tóth et al. 2011), single droplets (Al Zaitone and Lamprecht 2013; Davies et al. 2012; Jalaal and Mehravaran 2012; Liu et al. 2011a; Liu et al. 2011b; Schutyser et al. 2012), or monodisperse droplet chains (Azhdarzadeh et al. 2014; Gebel et al. 2015; Li et al. 2012). The method of droplets suspended on a thin filament may influence the evaporation process by affecting the heat conduction via the contact between the filament and the droplet. Secondly, filament techniques normally require droplets with diameters in the millimeter range, which undergo a different evaporation process compared to microdroplets relevant for inhalation applications (Schutyser et al. 2012). The single droplet method is based on droplets evaporating in either a falling gas flow (Jalaal and Mehravaran 2012; Lehmann et al. 2015) or in a quiescent environment (Chen et al. 2011; Davies et al. 2012; Wegener et al. 2014). The method of a single droplet falling in a gas flow is difficult

to apply for fast process such as the evaporation of a micro-droplet which lasts only a few milliseconds.

Single particle studies in a quiescent environment have led to important improvements in the understanding of concepts such as chemical reactivity, equilibrium particle size, and hygroscopicity (Wills et al. 2009). Furthermore, the single droplet method provides detailed information on the mechanisms that lead to the evaporation of the solvent from a solution droplet and the physical transformation of a particle through phase transformation and growth (Hopkins et al. 2004). The traditional technique to hold a droplet in a quiescent environment is using the effect of radiation pressure (Ashkin and Dziedzic 1975; Davis 1997; Schweiger 1990). If levitated with radiation pressure, the droplets experience a force in the direction of the laser beam propagation (Ashkin and Dziedzic 1975). A slight modification to this traditional technique is optical tweezers. Optical tweezers have been widely used in fields such as biology or colloidal science (McGloin 2006), but their utility in aerosol science has been emphasized by several recent studies (Hargreaves et al. 2010; Hopkins et al. 2004; Knox et al. 2010; Miles et al. 2012). The use of optical tweezers or optical traps eliminates the force balance problem encountered with the traditional radiation pressure technique. Optical tweezers focus the laser beam using a microscope objective forming a single beam gradient force trap, where the particle is attracted toward the region of highest light intensity and confined in three dimensions (Wills et al. 2009). A drawback of the single droplet method is the time required for the capture and the stabilization of the droplet. In addition, particles have to remain homogenous and spherical if cavity enhanced. Raman scattering is to be used to determine particle physical properties such as size and refractive index.

The droplet chain method is widely used in experimental studies of evaporation processes, not only in spray drying, but also in other areas such as microfluidics, MEMS, combustion, and colloids chemistry (Roger et al. 2013; Verboket et al. 2014; Vladisavljević et al. 2012; Waldron et al. 2014). A monodisperse droplet chain can be formed by injection of uniform droplets into a gas flow. Monodisperse droplets can be produced using a thermal dispenser, a vibrating orifice, or a piezoceramic dispenser. The piezoceramic dispenser is commonly used in recent studies due to several advantages. It typically does not generate interfering air bubbles, which are common in thermal dispensers (Sgro et al. 2007; Zhu and Power 2008). It can produce droplets with a spacing larger than several droplet diameters unlike the more narrowly spaced droplets from

vibrating orifices which may lead to droplets merging (Iida et al. 2014; Kosch and Ashgriz 2015).

Both monodisperse droplet chain and single droplet methods need a theoretical model to aid interpreting the experimental data. In this work, the theoretical particle formation model introduced by Vehring et al. (Vehring et al. 2007) is modified and implemented. This model provides a partial description of particle formation for cases that are dominated by liquid phase diffusion (Vehring et al. 2007). The model was extended to cases with very slow diffusion by Boraey et al. (Boraey and Vehring 2014). These models require a constant droplet evaporation rate. In the work presented here the model was adapted to allow for a change in material properties and evaporation rate over time. The goal of the present work is to describe the crystallization part of the particle formation process in more detail.

EXPERIMENTAL SECTION

Chemicals

Sodium nitrate ($NaNO_3$) (catalog number 221341-500G, Sigma Aldrich, St Louis, MO, USA) was used; its relevant properties, as listed by the manufacturer, are: true density of 2260 mg/ml, and purity greater than 99%. Glass transition temperature and melting point of $NaNO_3$ are 185 – 215°C and 306°C, respectively (Kracek et al. 1931). This solute was dissolved in deionized Water (DI H_2O) (catalog number 38796 – 1L, Sigma Aldrich, St Louis, MO, USA) with a residual content lower than 0.01%.

Experimental setup

Monodisperse droplet chain

The monodisperse droplet chain was generated using an experimental setup which has been described before (Baldelli et al. 2015). Briefly, it consisted of three main parts: feeding system, collection device, and optical setup, Figure 1. The feeding part consisted of a piezoceramic dispenser (MJ-ATP-01-30, MicroFab Technologies, Plano, Texas, USA) with an orifice diameter of 30 µm, a flow tube and minor components. The piezoceramic dispenser was controlled with a driver (MD-E-3000 Microdrop Technologies, Mühlenweg, Norderstedt, Germany), which allowed the applied voltage and frequency to be governed. Voltage and frequency influenced the speed of the first injected droplet and the number of droplets in the chain, respectively.

The flow tube had double walls with a partially evacuated gap for thermally insulating the internal gas flow. The square cross section of the flow tube improved the visualization of the whole particle formation process. Two heaters were located on the top of the flow tube to warm the air to a set temperature. The temperature values were recorded with two type K thermocouples (TFE-K-20, Omega Engineering, Laval, Quebec, Canada). The recording points were at the exit of the first heater and at the injection point. The gas flow rate was measured with a flow meter (4000 Series, TSI, Shoreview, Minnesota, U.S.). A low flow rate of 2 L/min was used to reduce the turbulence in the flow tube.

After the solution was filled into the dispenser, droplets were injected into a dry (< 1 % RH) laminar flow with controlled temperature. The distance between the injection point and the collection point was about 1 meter. This length allowed the use of a broader range of liquids, including liquids with low evaporation rate at low wet bulb temperatures. The collection device allowed the dried microparticles to be sampled on a hollowed Scanning Electron Microscope (SEM) substrate. The hollowed SEM stub was covered with filters with 0.2 µm pores (GTTP 013 00, Millipore Isopore Polycarbonate, Darmstadt, Germany). The microparticles were collected differently for the analysis of their solid phase by Raman spectroscopy (Wang et al. 2014). The filters were substituted with metal frits (Catalog number 9446T31, McMaster Carr, Aurora, OH, USA) with pores of an average diameter of 0.2 µm. All samples were stored in a dry environment until further analysis. Due to the high glass transition temperature of $NaNO_3$, solid phase transitions were unlikely to occur on the sample stubs. Collected particles were gold sputter coated with a vacuum desk sputter coater (Desk II, Denton Vacuum LLC., Moorestown, New Jersey, U.S.). The samples were then analyzed with an SEM (SEM LEO 1430, Zeiss, Jena, Germany) and a Focused Ion Beam Milling (FIB) (Hitachi NB 50000, Chiyoda, Tokyo, Japan) device. The images were analyzed using the software ImageJ, (ImageJ, Imaging Processing and Analysis in Java, National Institute of Health, 1997, Bethesda, Maryland, USA). The optical part consisted of a camera (BM-500 GE GigE Vision, Pleora Technologies, Kanata, Ontario, Canada) that recorded the droplet chain illuminated by a diode laser (SNF-660 Lasiris, Coherent Co., Wilsonville, Oregon, U.S.). In addition, the camera was free to move vertically from the injection to the collection point. For calibration purposes, a scale bar with a resolution of 1 mm was placed in the same plane as the monodisperse droplet chain.

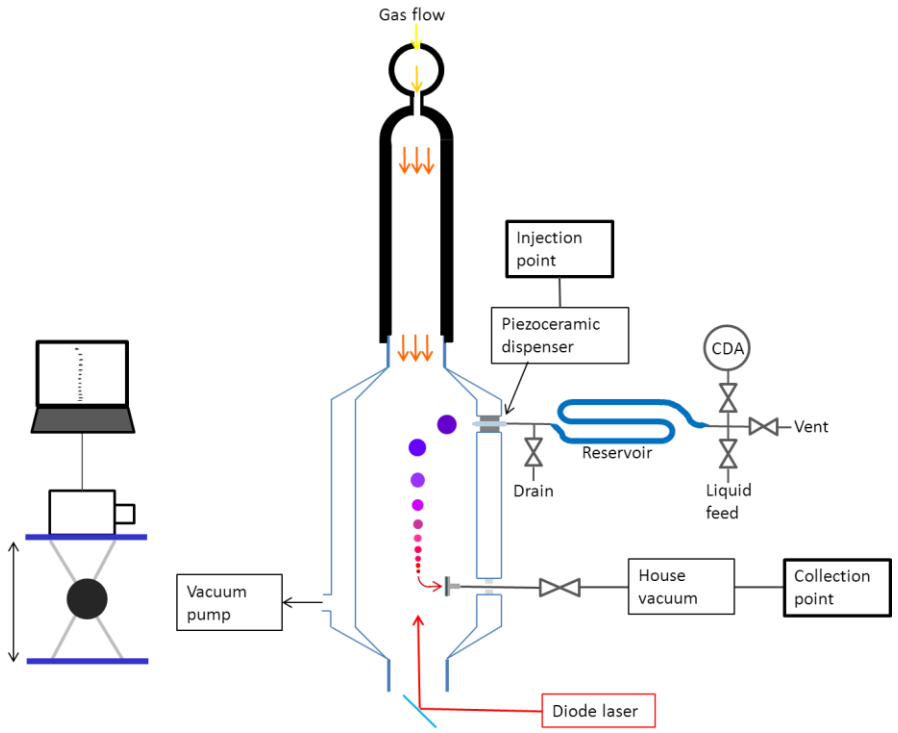

Figure 1 **Main components of the experimental setup. Liquid is fed to a piezoceramic dispenser, which produces a monodisperse droplet chain. This chain follows the streamline of a temperature regulated gas flow. Dried microparticles are collected at the bottom of the flow tube onto a Scanning Electron Microscope sample stub. The flow tube is double walled for insulation. The flow tube has a square cross section facilitating the recording of images of the droplet chain. The images are recorded using a pulsed diode laser that highlights the chain of droplets and a camera that can be moved vertically to image all the droplets in the chain.**

Determination of viscosity

The viscosities of aqueous solutions of sodium nitrate were determined as a function of mass fraction of solute by controllably inducing coalescence between two droplets held in holographic optical tweezers (Zheng et al. 2014). Details of the experimental technique are described in the supplementary information.

Figure 2 shows the trend of viscosity with sodium nitrate mass fraction, determined at 25ºC. The viscosity trend is essential for the derivation of the diffusion coefficient dependence with sodium nitrate mass fraction. The trend line shown in Figure 2 is used to calculate viscosity also for mass fraction higher than 0.85, which is an experimental limit. Results shown in Figure 2 agree with measurements of the viscosities achieved using aqueous solutions (Doan and Sangster 1981).

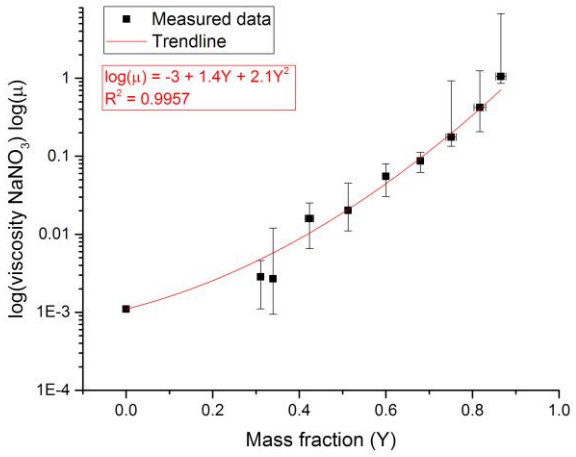

Figure 2 Viscosity as a function of mass fraction of sodium nitrate in an aqueous solution.

Measurement and derivation of the main parameters of the particle formation process

To describe the evaporation and particle formation process, aerodynamic diameter, volume equivalent diameter, particle density, and solute concentration are determined as a function of time. Images of the whole monodisperse droplet chain are analyzed to determine the distance between two consecutive droplets or particles. From the distance between two consecutive droplets their velocity can be obtained, because the production frequency of the droplets is known. Subtracting the velocity of the gas flow, which can be calculated from the volume flow rate and the geometry of the flow tube, yields the settling velocity, v_s of the droplets or particles as a function of position or time. The aerodynamic diameter, d_a, follows from the settling velocity. This method was introduced in a previous publication (Baldelli et al. 2015).

The volume equivalent diameter, d_v, as a function of time, t, can be determined if the particle density at every time step, i, is known. Depending on the phase of the particle formation process, the particle density, ρ_P, is approximated by different methods. Before any possible shell formation, it can be assumed that the particle is a sphere without internal voids. In this case, the mass fraction of the solute, Y_{sol}, in the particle is given by Equation 1.

$$Y_{\mathrm{sol}}(t) = \frac{M_{\mathrm{sol}}}{M(t)} = \frac{C_0 {d_{\mathrm{v},0}}^3}{\rho_{\mathrm{P}}(t) {d_{\mathrm{v,i}}}^3} = \frac{C_0 {d_{\mathrm{a},0}}^3}{\rho_{\mathrm{P}}(t) {d_{\mathrm{v,i}}}^3} \qquad \textbf{Equation 1}$$

in which $d_{a,0}$ is the aerodynamic diameter at the initial time step, M_{sol} the mass of solute in the droplet, and $M(t)$ is the total mass of the droplet or particle. Under the assumption that the droplet initially consists of a dilute aqueous solution with concentration, C_0, the particle density

is close to 1 kg/L. Therefore, the initial aerodynamic diameter can be replaced by the initial volume equivalent diameter, $d_{v,0}$. For a sphere with a diameter large enough such that non-continuum effects can be neglected the volume equivalent diameter can be substituted with Equation 2.

$$\frac{\rho^*}{\rho_P(t)} d_{a,i}^2 = d_{v,i}^2 \qquad \textbf{Equation 2}$$

where ρ^* is the standard density [1 kg/L]. Lastly, the density of a solution can be expressed as a function of the mass fraction of the solute based on measured data (Isono 1984; Mahiuddin and Ismail 1996) in the form shown in Equation 3.

$$Y_{sol}(t) = A\rho_P(t) - B \qquad \textbf{Equation 3}$$

The parameters *A* and *B* vary according to the wet bulb temperatures of the evaporating droplet. Values of *A* range from 0.0018 to 0.0021 ml/mg and values of *B* range from -2.06 to -1.94 (Isono 1984). Equation 4 is obtained by combining Equation 1, 2 and 3. Equation 4 can be solved iteratively for the particle density at each time step.

$$\rho_P(t) = \left(\frac{C_0 \rho_P^{\frac{1}{2}} {d_{a,0}}^3}{\rho^{*\frac{3}{2}} {d_{a,i}}^3} + B \right) \frac{1}{A} \qquad \textbf{Equation 4}$$

In the later phase of the particle formation a shell may have formed and the assumption of a sphere without voids is no longer valid. Also, the volume equivalent diameter of the particles cannot be smaller than the diameter of the final dried particles, d_f, In this phase the particle density can be approximated by a different method. Assuming that the volume equivalent diameter is now fixed at d_f, the particle density follows from Equation 5. The diameter of the final dried particles can be determined from an analysis of electromicrographs. Equation 5 is derived assuming that the volume equivalent diameter, after the shell formation, is constant and equal to the diameter of the final dried microparticles.

$$\rho_p(t) = \rho^* \left(\frac{d_{a,i}}{d_f} \right)^2 \qquad \textbf{Equation 5}$$

The shell thickness can also be approximated from the final particle diameter and the ratio of particle density to true density of the solute, ρ_T, as shown in Equation 6 (Boraey and Vehring 2014). In Equation 6, d_s indicates the diameter of the inner void in the final dried microparticle.

$$d_s = d_f \sqrt[3]{1 - \frac{\rho_p}{\rho_T}} \qquad \textbf{Equation 6}$$

Figure 3 shows a typical result for the aerodynamic diameter, measured using light scattering, as a function of time and the volume equivalent diameter derived using the methods described above. The next step in the analysis of the particle formation process requires knowledge of the evaporation rate of the droplets. The previously used steady-state particle formation model assumed that all variables are unaffected by a possible change of properties with time and assumed a constant evaporation rate (Baldelli et al. 2015). The dot-dashed line in Figure 3 is drawn connecting the initial volume equivalent diameter squared and the first occurrence of the final aerodynamic diameter. It is apparent that assuming a constant evaporation rate for this case would produce a large error in the derivation of related properties. Therefore, a variable evaporation rate was used for further analysis.

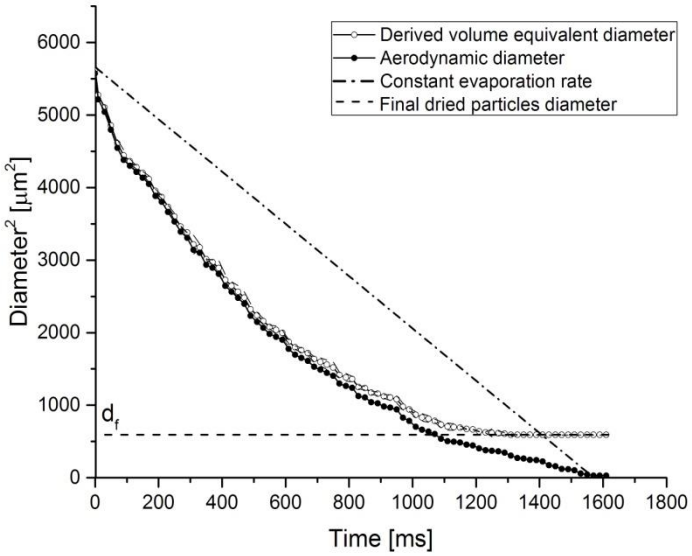

Figure 3 Determination of aerodynamic and volume equivalent diameter as a function of time in a droplet chain for a gas temperature of 25ºC and an initial concentration of 5 mg/ml. The dashed line represents the final diameter of the dried particles. The dash-dot line is an approximation for a hypothetical constant evaporation rate case.

The evaporation rate, κ, as a function of time is calculated as the slope of the volume equivalent diameter squared according to Equation 7.

$$\kappa\,(t) = \frac{{d_{\mathrm{v,i+1}}}^2 - {d_{\mathrm{v,i}}}^2}{t_{\mathrm{i+1}} - t_{\mathrm{i}}} \qquad \textbf{Equation 7}$$

Where $d_{\mathrm{v,i+1}}$ and $d_{\mathrm{v,i}}$ are the volume equivalent diameter at droplet i+1 and i, respectively. $t_{\mathrm{i+1}}$ and t_{i} are the time corresponding to droplet i+1 and i, respectively.

Previous publications have demonstrated that the Peclet number, *Pe*, is an indicator of the morphology of the final dried particles (Belotti et al. 2015; Castillo et al. 2014; Nuzzo et al. 2014). Larger Peclet numbers indicate low density particles, typically with a shell. Previously, the Peclet number was treated as constant. Here, the evaporation rate changes with time, Equation 8.

$$Pe(t) = \frac{\kappa(t)}{8D(t)} \qquad \textbf{Equation 8}$$

Since the restriction of constant Peclet number no longer applies, we can also admit a diffusion coefficient, $D(t)$, that changes over time. The diffusion coefficient is obtained from the viscosity, μ, of the solution using the Stokes Einstein equation (Ohtori and Ishii 2015), as shown in Equation 9.

$$D\,(t) = \frac{k_{\mathrm{B}} T_{\mathrm{w}}}{6\pi\mu(t) r} \qquad \textbf{Equation 9}$$

Where k_{B} is the Boltzmann's constant, T_{w} is the wet bulb temperature of the evaporating droplet and r the Stokes' radius of $NaNO_3$, 0.309 nm (Sata 2000).

The relationship between $NaNO_3$ mass fraction, Equation 1, and viscosity is provided from experimental results on coalescing droplets levitated in optical tweezers, described above. Power et al. (Power et al. 2013) have confirmed for sucrose solutions that the Stokes Einstein equation provides a reasonable method for estimating diffusion constants from viscosities when the viscosity is in the range 10^{-3} to 10 Pa s. Over this range, the estimated diffusion constant may be expected to be within one order of magnitude of the correct value.

The surface enrichment *E* is another important parameter for the evaluation of the particle formation process. It is defined as the surface concentration of the solute relative to its average concentration in the droplet, c_{m}. (Boraey and Vehring 2014). Equation 10 shows the relationship used to determine *E*. This equation has negligible error for Peclet numbers lower than 0.5. For higher Peclet numbers, the error related to the enrichment increases, but assuming a steady state system, Equation 10 can be used to approximate the enrichment for Peclet numbers up to 20. For

higher Peclet numbers, encountered towards the end of the evaporation process, Equation 11 provides an approximation (Boraey and Vehring 2014).

Pe < 20

$$E = 1 + \frac{Pe}{5} + \frac{Pe^2}{100} - \frac{Pe^3}{4000} \quad \textbf{Equation 10}$$

Pe > 20

$$E = \frac{Pe}{3} + \frac{4}{11} \quad \textbf{Equation 11}$$

The particle formation process cannot be fully explained without knowing the time required to reach saturation. The time to reach saturation is defined as the time at which the surface concentration reaches the solubility limit of the solute at a determined wet bulb temperature. The surface concentration is obtained using Equation 12.

$$c_{\mathrm{s}}(t) = E(t)\, c_{\mathrm{m}}(t) \quad \textbf{Equation 12}$$

However, it is known that crystallization does not start at saturation, but rather requires a certain level of supersaturation, depending on the nucleation mechanism. Hence, the time for crystallization defines the time at which the crystal starts to nucleate and subsequently grow. Tang and Munkelwitz (Tang and Munkelwitz 1994) studied the evaporation of sodium nitrate and other inorganic components using a single droplet evaporating in an electrodynamic balance. These authors reported that nucleation commences at a concentration between 83% to 98% of $NaNO_3$ by weight (Tang and Munkelwitz 1994). Because of the fast kinetics encountered in the drying of microdroplets, the time for crystallization was defined here as the time at which the $NaNO_3$ weight percentage reaches the higher value of 98%.

For simplification, two time intervals are introduced: the precipitation window (Δt_{p}) and the crystallization window (Δt_{c}). These two time intervals simplify the understanding and the explanation of the relationship between the final dried particle properties and the crystallization process. The Δt_{p} and Δt_{c} are the time between the time to reach saturation or the time for crystallization, respectively, and the time to reach constant aerodynamic diameter. The time for constant aerodynamic diameter is the time at which the aerodynamic diameter stops to decrease. At this point, it is assumed that all the solvent is evaporated.

RESULTS

For various initial conditions and the gas temperatures, Table 1 lists the predicted time intervals available for precipitation and crystallization, Δt_p and Δt_c, respectively. For the sake of brevity, further results are shown mostly for four or six representative cases, highlighted in Table 1. The four main cases are: 5 mg/ml at 50°C, $5 \cdot 10^{-1}$ mg/ml at 75°C, $5 \cdot 10^{-2}$ mg/ml at 100°C and $5 \cdot 10^{-4}$ mg/ml at 150°C. Two intermediate cases are added when a strong difference is highlighted; these two cases are $5 \cdot 10^{-3}$ mg/ml at 125°C and $5 \cdot 10^{-5}$ mg/ml at 150°C.

Table 1 **Experimental matrix with the predicted precipitation window (Δt_p) and crystallization window (Δt_c). The cases are distinguished by initial solution concentration (C_0) and drying gas temperature (T). The indicated errors were obtained by uncertainty propagation of the imaging resolution error.**

Co [mg/ml]	T [°C]	Δt_p [ms]	Δt_c [ms]	Co [mg/ml]	T [°C]	Δt_p [ms]	Δt_c [ms]
5	25	266 ± 2	265 ± 3	***5 × 10^{-3}***	25	132 ± 2	122 ± 5
	50	239 ± 2	221 ± 1		50	120 ± 1	110 ± 1
	75	221 ± 6	191 ± 3		75	101 ± 3	79 ± 1
	100	161 ± 4	122 ± 2		100	75 ± 2	73 ± 1
	125	119 ± 5	99 ± 2		***125***	37 ± 2	34 ± 2
	150	79 ± 14	60 ± 7		150	20 ± 1	16 ± 4
5 × 10^{-1}	25	190 ± 2	201 ± 1	***5 × 10^{-4}***	25	98 ± 2	82 ± 4
	50	181 ± 1	162 ± 17		50	80 ± 1	79 ± 2
	75	161 ± 3	151 ± 1		75	62 ± 5	49 ± 1
	100	119 ± 18	95 ± 4		100	56 ± 4	38 ± 2
	125	90 ± 5	68 ± 2		125	36 ± 1	22 ± 1
	150	62 ± 8	49 ± 12		***150***	16 ± 2	10 ± 8
5 × 10^{-2}	25	159 ± 1	144 ± 9	***5 × 10^{-5}***	25	78 ± 2	59 ± 1
	50	139 ± 7	138 ± 3		50	54 ± 2	36 ± 2
	75	117 ± 2	115 ± 1		75	36 ± 1	26 ± 1

100	99 ± 9	92 ± 2	100	20 ± 1	19 ± 1
125	59 ± 3	58 ± 2	125	18 ± 2	10 ± 1
150	39 ± 1	31 ± 5	***150***	5 ± 1	4 ± 1

Table 2 shows the morphology of the final dried particles. The Scanning Electron Microscope (SEM) images show the dimensions and the external morphology of the final dried particles. The ion beam milled (FIB) particles show the shell thickness and the internal morphology. Table 2 also lists the crystallization window and the final particle density for these cases. The values of density shown in Table 2 were derived from an analysis of SEM and FIB images. The final dried microparticles were monodisperse; thus, their properties, such as density, amount of voids, morphology and diameter, were the same for each case.

Table 2 **Focused Ion Beam (FIB) and Scanning Electron Microscope (SEM) images of the final dried microparticles. The cases are, from right to left, 5 mg/ml at 50°C, $5{\cdot}10^{-1}$ mg/ml at 75°C, $5{\cdot}10^{-2}$ mg/ml at 100°C and $5{\cdot}10^{-4}$ mg/ml at 150°C. Final particle density and crystallization window are shown for each case.**

FIB	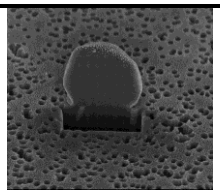	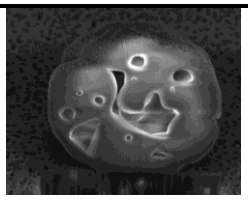	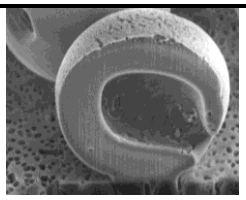	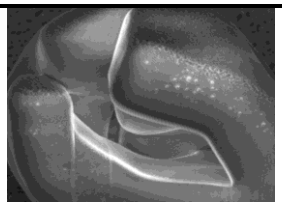
SEM	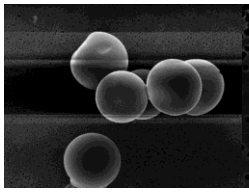	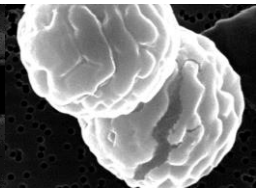	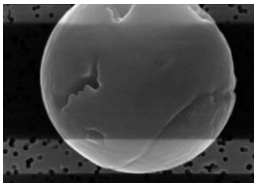	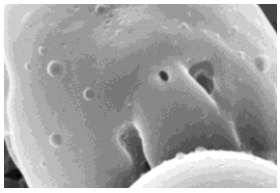
Scale bars	1 μm	1 μm	1 μm	1 μm
ρ_f [mg/ml]	1980	876	446	305
Δt_c [ms]	22	99	161	239

The FIB images show that the shell thickness changes with respect to the Δt_c. Table 3 shows the trend of Δt_c and amount of void space contained in the final dried particle. The void fraction was calculated using two methods: theoretical (Equation 6) and experimentally from the FIB images.

If the final dried particles contained several voids, it was assumed that all the voids were equally distributed along all directions and were concentrated at the center of the microparticles. The void fraction is calculated as the difference between the diameters of the equally distributed voids and the diameter of the final dried particles, derived from three separate SEM images.

Table 3 Comparison between predicted and experimentally observed void fractions of the final particles.

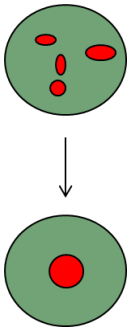

Δt_c [ms]	Void fraction (theoretical) [%]	Void fraction (experimental) [%]
37	34 ± 2	28 ± 10
99	61 ± 3	67 ± 20
161	80 ± 3	78 ± 13
239	90 ± 4	96 ± 6

The particle density, derived using Equation 4 and Equation 5, is shown in Figure 5 for three selected cases. Figure 5 shows the difference between the two equations used to calculate the density of droplets or particles, Equation 4 and Equation 5. Equation 4 is based on the assumption of droplets or particles without internal or external voids. Equation 5 takes advantage of the SEM analysis on the properties of the final dried microparticles. The crossing point of the two methods identifies the point at which the derived volume equivalent diameter is equal to the diameter of the final dried particles. The exact point in time at which voids first occur is unknown. Therefore, both versions are provided after the crossing point.

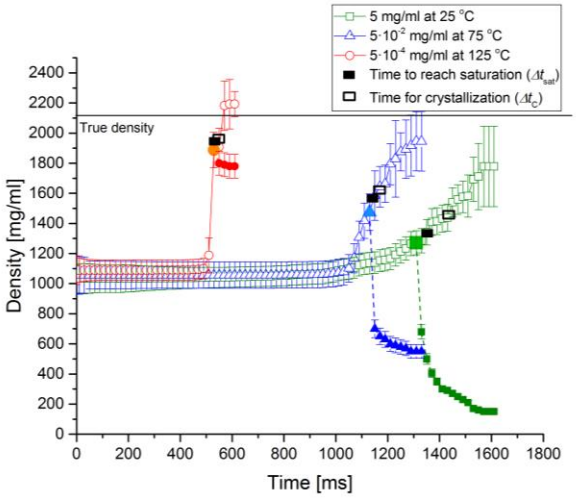

Figure 4 **Particle density as a function of time during the particle formation process for three sample cases, 5 mg/ml at 25°C, 5 × 10^{-2} mg/ml at 75°C and 5 × 10^{-4} mg/ml at 125°C. The full black squares show the predicted time to reach saturation and the empty black squares the predicted time for onset of crystallization. The right part of each curve, described with full symbols, is obtained using Equation 5. The part of the curves, described with empty symbols, is obtained using Equation 4.**

Figure 5 shows the predicted droplet surface concentration of sodium nitrate as a function of time. The plots are terminated at the saturation time point. The surface concentration curves allow determination of the time to reach saturation for every case considered. The dashed lines in Figure 5 indicate: horizontally, the solubility limit for the appropriate wet bulb temperature for each case and vertically, the time to reach saturation.

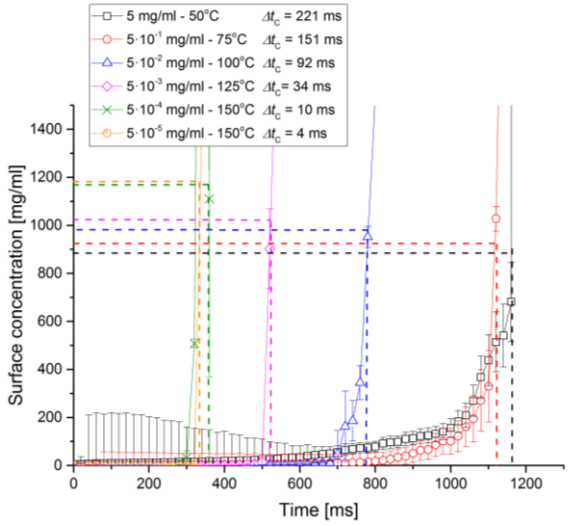

Figure 5 **Predicted droplet surface concentration of NaNO3 as a function of time during the evaporation process. The horizontal dashed lines indicate the solubility limit; the vertical dashed lines the**

time to reach saturation.

The trend of the normalized particle densities of the final dried microparticles as a function of crystallization window is shown in Figure 6. For larger crystallization windows, i.e. more time available for crystallization, the final particle densities are lower; for very small crystallization windows the normalized particle density approaches 1, indicating a solid particle without voids. This plot introduces the effect of the initial conditions to the crystallization window. Both initial solution concentration and temperatures of the external environment impact the properties of the final dried particles. Crystallization windows to the left of the dashed line labeled 'experimental limit' have large uncertainties due to the limited time resolution of the droplet chain method.

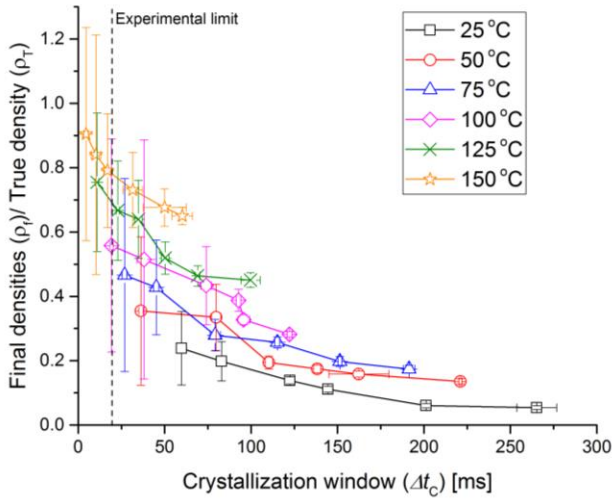

Figure 6 **Relationship between the predicted time available for crystallization, e and the final particle density normalized by the true density of the solute. For each line, the six data points are obtained increasing the concentration in the initial solution.**

Another instructive property of the final dried particles is the solid phase. As with the other properties, the solid state is affected by the Δt_c of the cases considered. Figure 7 shows the relationship between the crystallinity of the final microparticles and Δt_c. It has been shown that sodium nitrate can be considered mostly amorphous when the peaks at Raman shifts of 96 and 185 cm^{-1} disappear (Payne et al. 1997; Shen et al. 1975). These two Raman peaks at 96 and 185 cm^{-1} are caused by long-wavelength librational and transitional crystal lattice modes. To the left, the Raman spectra of six typical cases are shown. The peak areas of both the 185 cm^{-1} lattice peak and the 96 cm^{-1} lattice peak normalized by the peak area of a reference peak at 1067 cm^{-1}, caused by an intramolecular vibrational mode, are shown for all studied cases to the right. The

normalized peak area increases with Δt_c, indicating increasing order in the solid. The smallest Δt_c are correlated with mostly amorphous final dried particles.

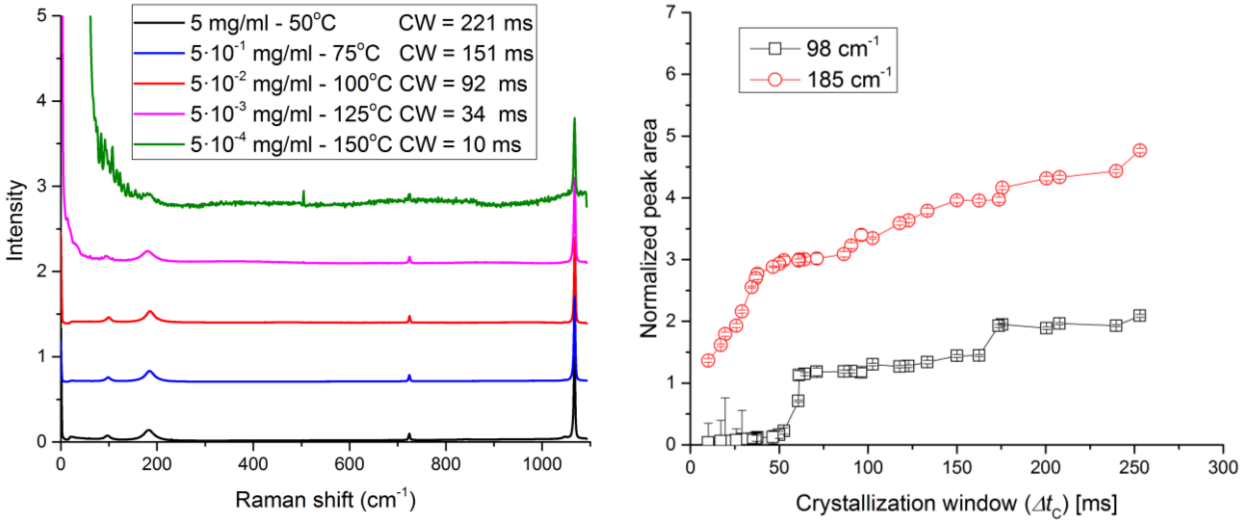

Figure 7 **Crystallinity of the final particles as a function of crystallization window. Raman spectra of six typical cases are shown in the left panel. The right panel shows the normalized peak area of the crystal lattice mode at 96 and 185 cm^{-1}, a measure of order in the solid phase.**

DISCUSSION

The purpose of this project is to understand the role of crystallization on particle formation. The main properties of the particle formation process are assessed through a combination of experimental tests and theoretical predictions. A time-variable model is necessary for the prediction of the main parameters of the particle formation process of a crystalline solute. The evaporation rate obtained with a time-constant model does not approximate the slope of the squared volume equivalent diameter, Figure 3.

The combination of the time-variable model and experimental results determine several parameters of the particle formation process, such as diameter, both aerodynamic and volume equivalent, density, mass, and void amount. The trend of diameters and density with time indicates the main phases of the particle formation process, such as solvent evaporation, shell formation and solute saturation. When the droplet is dilute, the aerodynamic and the volume equivalent diameter have similar values, Figure 3. Subsequently, the density curve reaches a peak, which indicates the shell formation point, Figure 4. After shell formation the volume equivalent diameter is assumed to be constant, but the aerodynamic diameter keeps decreasing. This shows that the solvent trapped inside a formed shell is evaporating through the shell's pores.

The density curve reaches a plateau only when the aerodynamic diameter becomes constant, Figure 4. The condition of supersaturation is reached between the time step indicating the shell formation and the next time step, Figure 5. Between these two time steps the surface concentration rises strongly, Figure 5.

The time for onset of crystallization and the remaining time available for crystallization, the crystallization window, are two variables that strongly influence the particle formation process. The initial process and formulation conditions of the particle formation process in turn influence the crystallization window. The largest values of the crystallization window are achieved in cases where the concentration of the initial solution is high and the temperature of the external environment is low. It is expected that increasing the relative humidity of the environment would have a similar effect. This would be the case for evaporation of ambient particles in the atmosphere. On the other hand, the smallest Δt_c is achieved for the combination of low concentration of the initial solution and high temperature of the external environment, Table 1. For the same temperature of the drying gas, the time for crystallization is reached later for lower initial concentration. For the same initial concentration, the time for crystallization is reached earlier for higher temperatures of the external environment. The temperature of the external environment influences the evaporation rate and thus surface saturation. The higher wet bulb temperature shortens the particle formation process. As a consequence, the crystallization window is also reduced. In addition, the surface concentration reaches saturation earlier in those cases, Figure 5.

The crystallization window influences the properties of the final dried microparticles. Smaller values of Δt_c produce microparticles with a smaller diameter, smaller crystal size, smoother surface, lower crystalline content and smaller void volume, Table 2, Table 3 and Figure 7. A smaller crystallization window indicates less time for the solute to nucleate and for crystals to grow. As a consequence, for smaller crystallization windows, the final microparticles appear mostly amorphous, Figure 7. Furthermore, both theoretical derivations (Boraey and Vehring 2014) and experimental results agree that for these cases the final dried microparticles have a smaller void fraction, Table 3. This agreement validates the theoretical derivations used.

For cases of high wet bulb temperatures and low concentration, the droplets show a high evaporation rate. The low solute mass fraction corresponds to low viscosity and a high diffusion coefficient. Previous publications on non-crytallizing systems show that for these conditions

amorphous particles are expected to have a thin shell and a larger diameter (Vehring et al. 2007). The crystallization event causes a different result. Here, shell formation is induced by the crystallization event. At a certain mass fraction, the solute starts to nucleate on the surface and subsequently generates a shell. This phase can be identified in a drastic drop in density curves, Figure 4. Close to this point in the evaporation process the theoretical model predicts that supersaturation is reached. Then, a long crystallization window allows these crystals to grow and form the shell of the final microparticles. The crystallization effect is emphasized by the gap between the density curves for time steps after the shell formation, Figure 4. For cases where the final dried particles are mostly amorphous, Table 2, the gap between the two methods is reduced, highlighting the impact of the crystallization on the particle formation process, mainly after the shell formation.

The methods used to analyze the particle formation process show limitations. These limitations are seen in both density curves and surface concentration curves, where the trend changes drastically between the time step of shell formation and the following one, Figure 4 and Figure 6. In these 20 milliseconds, time to reach saturation and time for crystallization are reached. Selecting a smaller time step might reduce these limitations.

CONCLUSION

This project demonstrates that the crystallization process influences the particle formation process in the case of substances that can crystallize within the same amount of time. The time gap between the onset of crystallization and the completion of drying contains the main steps in the particle formation process. Only during this time period may crystals nucleate and grow. Thus, the duration of the crystallization window determines the properties of the dried microparticles. Longer crystallization windows generate microparticles with higher crystallinity, larger crystal size, higher void fraction, and, consequently, lower density.

Understanding the relationship between the initial process conditions and the crystallization window, and thereby, the properties of the final dried particles is expected to improve control over the performance of microparticle based products. This may improve the efficiency of the delivery of drugs for respiratory diseases. The delivery efficiency of respiratory drugs, for example, depends on the diameter and the dispersibility of the spray dried microparticles. For instance, leucine, a much studied respiratory excipient, shows different properties according to

its solid state. Leucine needs to be in crystalline form to improve powder dispersibility (Feng et al. 2011).

Limitations are found both on the experimental and on the theoretical approach. In the experiments, a time step of 20 milliseconds is chosen. A shorter time step might help with a better definition of important time variables, such as the time to reach saturation and the time for crystallization. The theoretical approach yields only approximate results for the onset of the crystallization, due to limitations of the semi-analytical model. A fully numerical model seems more appropriate to describe particle formation processes that involve crystallization.

ACKNOWLEDGEMENT

Funding from the Natural Sciences and Engineering Research Council of Canada (NSERC) and the Alberta Innovates Technology Futures is gratefully acknowledged. The authors thank Jason Dibbs for the fabrication of components of the setup used. JPR, RMP and REHM thank the EPSRC for financial support through a Leadership Fellowship awarded to JPR (grant reference EP/G007713/1) and grant EP/L010569/1.

REFERENCE

Al Zaitone, B. and Lamprecht, A. (2013). Single Droplet Drying Step Characterization in Microsphere Preparation. Colloids and Surfaces B: Biointerfaces 105:328-334.
Al Zaitone, B. A. and Tropea, C. (2011). Evaporation of Pure Liquid Droplets: Comparison of Droplet Evaporation in an Acoustic Field Versus Glass-Filament. Chemical Engineering Science 66:3914-3921.
Ashkin, A. and Dziedzic, J. (1975). Optical Levitation of Liquid Drops by Radiation Pressure. Science 187:1073-1075.
Azhdarzadeh, M., Olfert, J. S., Vehring, R., Finlay, W. H. (2014). Effect of Electrostatic Charge on Oral-Extrathoracic Deposition for Uniformly Charged Monodisperse Aerosols. Journal of Aerosol Science 68:38-45.
Baldelli, A., Boraey, M. A., Nobes, D. S., Vehring, R. (2015). Analysis of the Particle Formation Process of Structured Microparticles. Molecular Pharmaceutics 12:2562-2573.
Beck-Broichsitter, M., Merkel, O. M., Kissel, T. (2012). Controlled Pulmonary Drug and Gene Delivery Using Polymeric Nano-Carriers. Journal of Controlled Release 161:214-224.
Belotti, S., Rossi, A., Colombo, P., Bettini, R., Rekkas, D., Politis, S., Colombo, G., Balducci, A. G., Buttini, F. (2015). Spray-Dried Amikacin Sulphate Powder for Inhalation in Cystic Fibrosis Patients: The Role of Ethanol in Particle Formation. European Journal of Pharmaceutics and Biopharmaceutics 93:165-172.
Boraey, M. A. and Vehring, R. (2014). Diffusion Controlled Formation of Microparticles. Journal of Aerosol Science 67:131-143.
Bück, A., Palis, S., Tsotsas, E. (2015). Model-Based Control of Particle Properties in Fluidised Bed Spray Granulation. Powder Technology 270:575-583.

Byrn, S., Pfeiffer, R., Stephenson, G., Grant, D., Gleason, W. (1994). Solid-State Pharmaceutical Chemistry. Chemistry of Materials 6:1148-1158.
Castillo, J. L., Martin, S., Rodriguez-Perez, D., Perea, A., Garcia-Ybarra, P. L. (2014). Morphology and Nanostructure of Granular Materials Built from Nanoparticles. Kona Powder and Particle Journal:214-233.
Chen, W.-H., Hou, Y.-L., Hung, C.-I. (2011). A Theoretical Analysis of the Capture of Greenhouse Gases by Single Water Droplet at Atmospheric and Elevated Pressures. Applied Energy 88:5120-5130.
Courrier, H., Butz, N., Vandamme, T. F. (2002). Pulmonary Drug Delivery Systems: Recent Developments and Prospects. Critical Reviews™ in Therapeutic Drug Carrier Systems 19:425-498.
Davies, J. F., Haddrell, A. E., Miles, R. E., Bull, C. R., Reid, J. P. (2012). Bulk, Surface, and Gas-Phase Limited Water Transport in Aerosol. The Journal of Physical Chemistry A 116:10987-10998.
Davis, E. J. (1997). A History of Single Aerosol Particle Levitation. Aerosol Science and Technology 26:212-254.
Doan, T. H. and Sangster, J. (1981). Viscosities of Concentrated Aqueous Solutions of Some 1: 1, 2: 1, and 3: 1 Nitrates at 25. Degree. C. Journal of Chemical and Engineering Data 26:141-144.
Duprat, C., Bick, A. D., Warren, P. B., Stone, H. A. (2013). Evaporation of Drops on Two Parallel Fibers: Influence of the Liquid Morphology and Fiber Elasticity. Langmuir 29:7857-7863.
Elkordy, A. A., Forbes, R. T., Barry, B. W. (2004). Stability of Crystallised and Spray-Dried Lysozyme. International Journal of Pharmaceutics 278:209-219.
Everard, M. L., Clark, A. R., Milner, A. D. (1992). Drug Delivery from Jet Nebulisers. Archives of Disease in Childhood 67:586-591.
Feng, A., Boraey, M., Gwin, M., Finlay, P., Kuehl, P., Vehring, R. (2011). Mechanistic Models Facilitate Efficient Development of Leucine Containing Microparticles for Pulmonary Drug Delivery. International Journal of Pharmaceutics 409:156-163.
Garcia, A., Mack, P., Williams, S., Fromen, C., Shen, T., Tully, J., Pillai, J., Kuehl, P., Napier, M., DeSimone, J. M. (2012). Microfabricated Engineered Particle Systems for Respiratory Drug Delivery and Other Pharmaceutical Applications. Journal of Drug Delivery 2012.
Gebel, G., Mosbach, T., Meier, W., Aigner, M. (2015). Laser-Induced Blast Waves in Air and Their Effect on Monodisperse Droplet Chains of Ethanol and Kerosene. Shock Waves:1-15.
Gradon, L. and Sosnowski, T. R. (2014). Formation of Particles for Dry Powder Inhalers. Advanced Powder Technology 25:43-55.
Hargreaves, G., Kwamena, N.-O., Zhang, Y., Butler, J., Rushworth, S., Clegg, S., Reid, J. (2010). Measurements of the Equilibrium Size of Supersaturated Aqueous Sodium Chloride Droplets at Low Relative Humidity Using Aerosol Optical Tweezers and an Electrodynamic Balance. The Journal of Physical Chemistry A 114:1806-1815.
Hoe, S., Ivey, J. W., Boraey, M. A., Shamsaddini-Shahrbabak, A., Javaheri, E., Matinkhoo, S., Finlay, W. H., Vehring, R. (2014). Use of a Fundamental Approach to Spray-Drying Formulation Design to Facilitate the Development of Multi-Component Dry Powder Aerosols for Respiratory Drug Delivery. Pharmaceutical Research 31:449-465.
Hopkins, R. J., Mitchem, L., Ward, A. D., Reid, J. P. (2004). Control and Characterisation of a Single Aerosol Droplet in a Single-Beam Gradient-Force Optical Trap. Physical Chemistry Chemical Physics 6:4924-4927.

Iida, K., Sakurai, H., Saito, K., Ehara, K. (2014). Inkjet Aerosol Generator as Monodisperse Particle Number Standard. Aerosol Science and Technology 48:789-802.
Isono, T. (1984). Density, Viscosity, and Electrolytic Conductivity of Concentrated Aqueous Electrolyte Solutions at Several Temperatures. Alkaline-Earth Chlorides, Lanthanum Chloride, Sodium Chloride, Sodium Nitrate, Sodium Bromide, Potassium Nitrate, Potassium Bromide, and Cadmium Nitrate. Journal of Chemical and Engineering Data 29:45-52.
Jalaal, M. and Mehravaran, K. (2012). Fragmentation of Falling Liquid Droplets in Bag Breakup Mode. International Journal of Multiphase Flow 47:115-132.
Knox, K. J., Burnham, D. R., McCann, L. I., Murphy, S. L., McGloin, D., Reid, J. P. (2010). Observation of Bistability of Trapping Position in Aerosol Optical Tweezers. JOSA B 27:582-591.
Kosch, S. and Ashgriz, N. (2015). Note: A Simple Vibrating Orifice Monodisperse Droplet Generator Using a Hard Drive Actuator Arm. Review of Scientific Instruments 86:046101.
Kracek, F., Posnjak, E., Hendricks, S. (1931). Gradual Transition in Sodium Nitrate. Ii. The Structure at Various Temperatures and Its Bearing on Molecular Rotation. Journal of the American Chemical Society 53:3339-3348.
Labiris, N. and Dolovich, M. (2003). Pulmonary Drug Delivery. Part I: Physiological Factors Affecting Therapeutic Effectiveness of Aerosolized Medications. British Journal of Clinical Pharmacology 56:588-599.
Lehmann, S., Lorenz, S., Rivard, E., Brüggemann, D. (2015). Experimental Analysis and Semicontinuous Simulation of Low-Temperature Droplet Evaporation of Multicomponent Fuels. Experiments in Fluids 56:1-12.
Li, Y., Zhang, S., Li, J. (2012). Indirect-Mode Jet Pulse Spray System Design and Monodisperse Droplets Generation. Chemical Engineering Science 68:461-468.
Liu, W., Wu, W., Selomulya, C., Chen, X. D. (2011a). A Single Step Assembly of Uniform Microparticles for Controlled Release Applications. Soft Matter 7:3323-3330.
Liu, W., Wu, W. D., Selomulya, C., Chen, X. D. (2011b). Facile Spray-Drying Assembly of Uniform Microencapsulates with Tunable Core–Shell Structures and Controlled Release Properties. Langmuir 27:12910-12915.
Mahiuddin, S. and Ismail, K. (1996). Temperature and Concentration Dependence of the Viscocity of Aqueous Sodium Nitrate and Sodium Thiosulphate Electrolytic Systems. Fluid Phase Equilibria 123:231-243.
McGloin, D. (2006). Optical Tweezers: 20 Years On. Philosophical Transactions of the Royal Society of London A: Mathematical, Physical and Engineering Sciences 364:3521-3537.
Miles, R. E., Walker, J. S., Burnham, D. R., Reid, J. P. (2012). Retrieval of the Complex Refractive Index of Aerosol Droplets from Optical Tweezers Measurements. Physical Chemistry Chemical Physics 14:3037-3047.
Nuzzo, M., Millqvist-Fureby, A., Sloth, J., Bergenstahl, B. (2014). Surface Composition and Morphology of Particles Dried Individually and by Spray Drying. Drying Technology 33:757-767.
Ohtori, N. and Ishii, Y. (2015). Explicit Expression for the Stokes-Einstein Relation for Pure Lennard-Jones Liquids. Physical Review E 91:012111.
Park, C.-W., Li, X., Vogt, F. G., Hayes, D., Zwischenberger, J. B., Park, E.-S., Mansour, H. M. (2013). Advanced Spray-Dried Design, Physicochemical Characterization, and Aerosol Dispersion Performance of Vancomycin and Clarithromycin Multifunctional Controlled Release Particles for Targeted Respiratory Delivery as Dry Powder Inhalation Aerosols. International Journal of Pharmaceutics 455:374-392.

Paudel, A., Worku, Z. A., Meeus, J., Guns, S., Van den Mooter, G. (2013). Manufacturing of Solid Dispersions of Poorly Water Soluble Drugs by Spray Drying: Formulation and Process Considerations. International Journal of Pharmaceutics 453:253-284.
Payne, S., Harris, M., Hagen, M., Dove, M. (1997). A Neutron Diffraction Study of the Order-Disorder Phase Transition in Sodium Nitrate. Journal of Physics: Condensed Matter 9:2423.
Power, R., Simpson, S., Reid, J., Hudson, A. (2013). The Transition from Liquid to Solid-Like Behaviour in Ultrahigh Viscosity Aerosol Particles. Chemical Science 4:2597-2604.
Roger, K., Botet, R., Cabane, B. (2013). Coalescence of Repelling Colloidal Droplets: A Route to Monodisperse Populations. Langmuir 29:5689-5700.
Sata, T. (2000). Studies on Anion Exchange Membranes Having Permselectivity for Specific Anions in Electrodialysis—Effect of Hydrophilicity of Anion Exchange Membranes on Permselectivity of Anions. Journal of Membrane Science 167:1-31.
Schutyser, M. A., Perdana, J., Boom, R. M. (2012). Single Droplet Drying for Optimal Spray Drying of Enzymes and Probiotics. Trends in Food Science & Technology 27:73-82.
Schweiger, G. (1990). Raman Scattering on Single Aerosol Particles and on Flowing Aerosols: A Review. Journal of Aerosol Science 21:483-509.
Sgro, A. E., Allen, P. B., Chiu, D. T. (2007). Thermoelectric Manipulation of Aqueous Droplets in Microfluidic Devices. Analytical Chemistry 79:4845-4851.
Shen, T., Mitra, S., Prask, H., Trevino, S. (1975). Order-Disorder Phenomenon in Sodium Nitrate Studied by Low-Frequency Raman Scattering. Physical Review B 12:4530.
Sou, T., Kaminskas, L. M., Nguyen, T.-H., Carlberg, R., McIntosh, M. P., Morton, D. A. (2013). The Effect of Amino Acid Excipients on Morphology and Solid-State Properties of Multi-Component Spray-Dried Formulations for Pulmonary Delivery of Biomacromolecules. European Journal of Pharmaceutics and Biopharmaceutics 83:234-243.
Steckel, H., Rasenack, N., Müller, B. W. (2003). In-Situ-Micronization of Disodium Cromoglycate for Pulmonary Delivery. European Journal of Pharmaceutics and Biopharmaceutics 55:173-180.
Tang, I. and Munkelwitz, H. (1994). Water Activities, Densities, and Refractive Indices of Aqueous Sulfates and Sodium Nitrate Droplets of Atmospheric Importance. Journal of Geophysical Research: Atmospheres (1984–2012) 99:18801-18808.
Ticehurst, M. D. and Marziano, I. (2015). Integration of Active Pharmaceutical Ingredient Solid Form Selection and Particle Engineering into Drug Product Design. Journal of Pharmacy and Pharmacology 67:782-802.
Tóth, T., Ferraro, D., Chiarello, E., Pierno, M., Mistura, G., Bissacco, G., Semprebon, C. (2011). Suspension of Water Droplets on Individual Pillars. Langmuir 27:4742-4748.
Vehring, R., Foss, W. R., Lechuga-Ballesteros, D. (2007). Particle Formation in Spray Drying. Journal of Aerosol Science 38:728-746.
Verboket, P. E., Borovinskaya, O., Meyer, N., Günther, D., Dittrich, P. S. (2014). A New Microfluidics-Based Droplet Dispenser for Icpms. Analytical Chemistry 86:6012-6018.
Vicente, J., Pinto, J., Menezes, J., Gaspar, F. (2013). Fundamental Analysis of Particle Formation in Spray Drying. Powder Technology 247:1-7.
Vladisavljević, G., Kobayashi, I., Nakajima, M. (2012). Production of Uniform Droplets Using Membrane, Microchannel and Microfluidic Emulsification Devices. Microfluidics and Nanofluidics 13:151-178.
Wachtel, H. (2016). Respiratory Drug Delivery, in Microsystems for Pharmatechnology, Springer, 257-274.

Waldron, K., Wu, W. D., Wu, Z., Liu, W., Selomulya, C., Zhao, D., Chen, X. D. (2014). Formation of Monodisperse Mesoporous Silica Microparticles Via Spray-Drying. Journal of Colloid and Interface Science 418:225-233.
Wang, H., Boraey, M. A., Williams, L., Lechuga-Ballesteros, D., Vehring, R. (2014). Low-Frequency Shift Dispersive Raman Spectroscopy for the Analysis of Respirable Dosage Forms. International Journal of Pharmaceutics 469:197-205.
Wegener, M., Paul, N., Kraume, M. (2014). Fluid Dynamics and Mass Transfer at Single Droplets in Liquid/Liquid Systems. International Journal of Heat and Mass Transfer 71:475-495.
Wills, J. B., Knox, K. J., Reid, J. P. (2009). Optical Control and Characterisation of Aerosol. Chemical Physics Letters 481:153-165.
Ye, X., Liu, Y., Lv, Y., Liu, G., Zheng, X., Han, Q., Jackson, K. A., Tao, X. (2015). In Situ Microscopic Observation of the Crystallization Process of Molecular Microparticles by Fluorescence Switching. Angewandte Chemie 127:8087–8091.
Zheng, X.-S., Hu, P., Zhong, J.-H., Zong, C., Wang, X., Liu, B.-J., Ren, B. (2014). Laser Power Dependent Surface-Enhanced Raman Spectroscopic Study of 4-Mercaptopyridine on Uniform Gold Nanoparticle-Assembled Substrates. The Journal of Physical Chemistry C 118:3750-3757.
Zhu, B., Traini, D., Lewis, D. A., Young, P. (2014). The Solid-State and Morphological Characteristics of Particles Generated from Solution-Based Metered Dose Inhalers: Influence of Ethanol Concentration and Intrinsic Drug Properties. Colloids and Surfaces A: Physicochemical and Engineering Aspects 443:345-355.
Zhu, Y. and Power, B. E. (2008). Lab-on-a-Chip in Vitro Compartmentalization Technologies for Protein Studies, in Protein–Protein Interaction, Springer, 81-114.